ADVANCED ELECTRONIC MATERIALS
www.advelectronicmat.de

Scandium Nitride as a Gateway III-Nitride Semiconductor for both Excitatory and Inhibitory Optoelectronic Artificial Synaptic Devices

*Dheemahi Rao, Ashalatha Indiradevi Kamalasanan Pillai, Magnus Garbrecht, and Bivas Saha**

Traditional computation based on von Neumann architecture is limited by time and energy consumption due to data transfer between the storage and the processing units. The von Neumann architecture is also inefficient in solving unstructured, probabilistic, and real-time problems. To address these challenges, a new brain-inspired neuromorphic computational architecture is required. Due to the absence of resistance–capacitance delay, high bandwidth, and low power consumption, optoelectronic artificial synaptic devices are highly attractive. Yet, stable, scalable, and complementary metal–oxide–semiconductor (CMOS)-compatible materials exhibiting both inhibitory and excitatory optoelectronic synaptic functionalities have not been demonstrated. Here, epitaxial CMOS-compatible scandium nitride (ScN) optoelectronic artificial synaptic devices that emulate both inhibitory and excitatory biological synaptic activities are presented. The negative and positive persistent photoconductivity of undoped and magnesium-doped ScN is equated to the inhibitory and excitatory synaptic plasticity, respectively, which leads to functionalities like learning–forgetting, frequency-selective optical filtering, frequency-dependent potentiation and depression, Hebbian learning, and logic-gate operations. Temperature-dependent photoresponse and photo-Hall measurements reveal that scattering of photogenerated carriers from charged defect centers results in negative photoconductivity in undoped degenerate ScN. This work opens up the possibility of utilizing a group-III epitaxial semiconducting nitride material with inhibitory and excitatory optoelectronic synaptic functionalities for practical neuromorphic applications.

1. Introduction

Conventional von Neumann computational architecture physically partitions memory and central processing units that result in extensive time delay and high energy consumption. Moreover, the von Neumann computational architecture is inept at addressing mathematically ill-defined, nonlinear, and stochastic problems, and requires complex algorithms that exert enormous resource constraints for handling big data in machine learning applications.[1,2] On the other hand, human brains are designed to solve complex spatio-temporal problems in real-time with far less energy consumption, and a significant degree of fault tolerance. Their superior performance is primarily derived from the highly parallel, distributed, and event-driven computational architecture.[3] Therefore, mimicking brain operation to develop the next generations of computational architecture has gained significant attraction for over three to four decades. A human brain contains ≈10^{11} neurons that are interconnected with ≈10^{15} synapses.[4] In each synapse, neurotransmitters are released from the pre-synaptic neuron in response to the action potential and flow

D. Rao
Chemistry and Physics of Materials Unit,
and International Centre for Materials Science
Jawaharlal Nehru Centre for Advanced Scientific Research
Bangalore 560064, India

The ORCID identification number(s) for the author(s) of this article can be found under https://doi.org/10.1002/aelm.202200975.

DOI: 10.1002/aelm.202200975

A. I. K. Pillai, M. Garbrecht
Sydney Microscopy and Microanalysis
The University of Sydney
NSW 2006, Australia

B. Saha
Chemistry and Physics of Materials Unit
International Centre for Materials Science,
and School of Advanced Materials (SAMat)
Jawaharlal Nehru Centre for Advanced Scientific Research
Bangalore 560064, India
E-mail: bsaha@jncasr.ac.in

through the synaptic cleft to the post-synaptic neuron, where the receptors detect them. Synapses are responsible for all the computation and memory in the brain. Therefore, mimicking the functionalities of the biological synaptic connection lies at the heart of the development of brain-inspired computational hardware.

Though von Neumann identified the similarities between the conventional computer architecture and the human central nervous system and tried to bring out a mathematical underpinning between the two, his untimely death in 1967 halted the substantial progress in the field for some time.[5] However, since the theoretical proposal by Carver Mead in the 1980s,[6] brain-inspired neuromorphic circuits have been developed on conventional complementary metal–oxide–semiconductor (CMOS) chips to emulate the synaptic functions, for example, TrueNorth chip from IBM[7] and Loihi chip from Intel.[8] However, such neuromorphic integrated circuits are incredibly power-hungry, limiting their utility in cloud-based computing operations and requiring a huge number of feedback loop operations to perform simple functions such as image and voice recognition. Such large room-sized computers are also not a viable alternative to the human brain, and in recent reports, these neuromorphic circuits are also demonstrated to be prone to be biased to their training data and are found to discriminate between races and genders.[9] Therefore, though the CMOS-based neuromorphic computing technology has made great progress over the last 10–15 years, brain-inspired neuromorphic hardware technologies needs to be developed that emulates the synaptic connections in brain with significantly reduced computational power and size.[10]

With the demonstration of memristor by the HP labs in 2008,[11] non-volatile memory-based artificial synaptic hardware connections have gained significant attention. The history-dependent resistive switching memristor functionalities are demonstrated in several materials such as metal oxides,[12] organic materials,[13] perovskites,[14] and 2D materials including graphene, h-BN, MoS_2, and WS_2.[15–17] Similarly, atomic-switching memory devices with Ag_2S,[18] ferroelectric tunnel junction devices,[19] and self-forming Ag networks[20] are also utilized to demonstrate the artificial synaptic functions. However, such devices are fully electrical and suffer from RC delays from interconnects, low bandwidth, and power losses. To address these shortcomings, all photonic synaptic devices that combine neural networks' efficiency and the speed of light have been developed based on phase-change materials like gallium lanthanum oxysulfide microfibers[21] and germanium antimony telluride.[22] Nevertheless, such fully optical synapses require complex wavelength conversion and expensive laser systems that are not feasible for practical applications. Therefore, opto-electrical artificial synapses that utilize persistent photoconductivity in semiconducting materials are proposed that offer bidirectional conversion between the electrical and optical signals.[23] Such photoelectric synapses exhibit wide bandwidth, lower RC delay, and power consumption. They can also integrate visual sensing, signal processing, and memorizing that closely emulate the human biological visual cortex system.

Optoelectronic artificial synaptic devices made up of metal oxides,[24] halide perovskites,[25] carbon nanotube heterostructures,[26] organic heterojunctions,[27] nanocrystals,[28] and 2D-MoS_2[29] have successfully mimicked the primary biological neural functions like short-term memory (STM), long-term memory (LTM), paired-pulse facilitation (PPF), and spike-timing-dependent plasticity (STDP). For artificial neural network application, tasks such as learning–forgetting,[24] classical conditioning,[24,27] latent inhibition,[24] aversion,[28] logic functions,[27,28] dynamic filtering,[29,30] and pattern sensing and memorizing[27] are demonstrated in some of these optoelectronic artificial synaptic devices. While such proof of concept demonstration has invigorated the optoelectronic artificial synapse research field, for practical device implementations where the artificial synapse-based neural circuits will have to be integrated into the CMOS chips (at least in the initial stages of development), stable, scalable, CMOS-compatible, and robust materials are required. Moreover, for practical device implementations, it is also necessary that the host material exhibit both the inhibitory and excitatory optoelectronic synaptic functionalities that most materials do not exhibit. Wurtzite III-nitride semiconductors, such as GaN, InN, and AlN are stable, CMOS processable, scalable, and attractive for a wide range of optoelectronic applications. However, their fast carrier recombination rate and little persistent photoconductivity are not commensurate for developing optoelectronic synapses.[31,32]

Scandium nitride (ScN) is an emerging group-III (B) semiconducting nitride that crystallizes in the rock salt structure with octahedral coordination, and is stable in ambient conditions with high mechanical hardness.[33] ScN has found significant interest for its thermoelectric properties,[34] as a substrate for defect-free GaN growth,[35] and as a semiconductor in metal/semiconductor superlattice development.[36] ScN exhibits an indirect bandgap of ≈0.9 eV and a direct bandgap of ≈2.2 eV.[37,38] ScN thin films are highly degenerate due to the presence of oxygen as impurity (O_N) and nitrogen vacancies (V_N) exhibiting a carrier concentration in ≈(1–4) × 10^{20} cm^{-3} range.[39,40] ScN thin films exhibit mobility between 20–120 cm^2 V^{-1} s^{-1} at room temperature depending on the growth conditions.[41–43] Recent research has also showed that ScN exhibits infrared plasmon and phonon-polaritons with high figures-of-merit.[44] Mg doping is found to be effective in reducing the high electron concentration, and p-type ScN thin films have been demonstrated that also exhibit high thermoelectric power factor.[45]

This work utilizes persistent negative photoconductivity (NPC) in intentionally undoped ScN, and persistent positive photoconductivity (PPC) in Mg-doped ScN thin films to develop inhibitory and excitatory optoelectronic artificial synapses, respectively. These artificial synapses exhibit STM and LTM, transitions from STM-to-LTM, learning, frequency-controlled PPF and paired-pulse depression (PPD), dynamic filtering, symmetric STDP, and logic gate operations. Temperature-dependent photoconductivity and photo-Hall measurements are further performed to explain the underlying device operation mechanism.

2. Results and Discussion

Intentionally undoped ScN and Mg-doped ScN thin films are deposited on (001) MgO substrates with reactive magnetron sputtering in an ultrahigh vacuum chamber. Without any intentional doping, the ScN film has electron concentration of

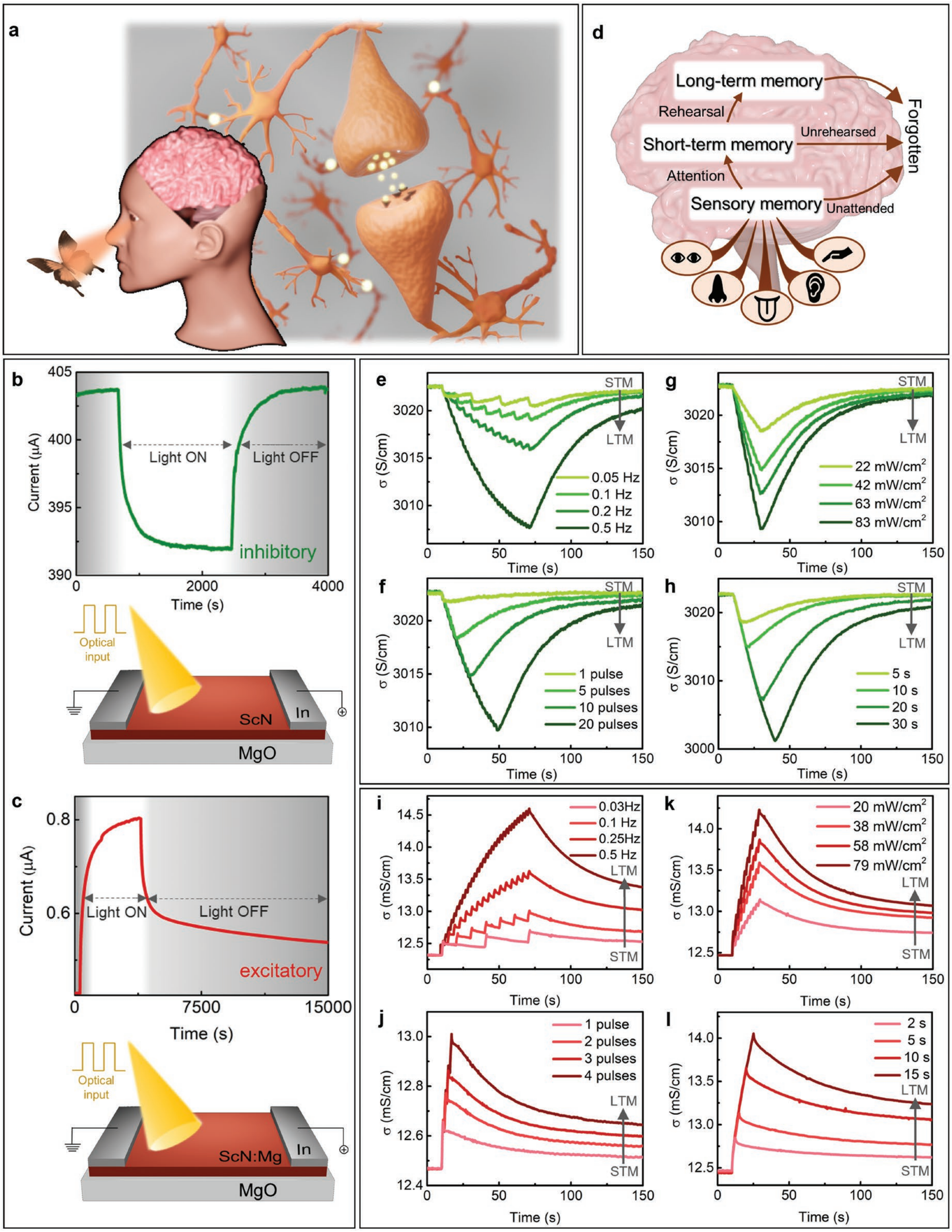

Figure 1. a) Schematic of human visual system and the neural synapse. b) Negative photoconductivity in ScN thin film measured in the device geometry shown below. At the onset of illumination, the current starts to decrease gradually and saturates within 30 min. After the light is turned off, the current takes about 15 min to return to its initial value. c) Positive photoconductivity in Mg-doped ScN thin film is measured in the device geometry shown below. At the onset of illumination, the current starts to increase gradually and does not saturate till 60 min. After turning off the light, the current takes longer than 3 h to return to its initial value. d) Atkinson–Shiffrin memory model proposing three main stages of memory in the human brain. e–h) Transition from STM to LTM in inhibitory ScN synapse as a function of frequency, number, intensity, and duration of optical pulses. i–l) Transition from STM to LTM in excitatory Mg-doped ScN synapse as a function of frequency, number, intensity, and duration of optical pulses.

2×10^{20} cm^{-3} and 63 cm^2 V^{-1} s^{-1} mobility. O_N and V_N act as unintentional n-type dopants in ScN, making it a degenerate semiconductor. With Mg(hole)-doping, the electron concentration is reduced to $\approx 2 \times 10^{18}$ cm^{-3}, and at higher Mg concentration holes become the majority carriers. Two-terminal devices are fabricated with indium (In) Ohmic contacts. Methods and the supporting information include details on the growth, characterization, device fabrication, and measurements.

The external stimuli sensed by the sensory organs generate an action potential that will release the neurotransmitters from the pre-synapse (**Figure 1**a). Depending on their role, these neurotransmitters will either increase (excitatory) or decrease (inhibitory) the likelihood of depolarization and generation of the action potential at the post-synapse. Figure 1b shows that undoped ScN exhibits negative photoconductivity, where the current decreases on illumination. After switching off the light, the current takes several minutes to return to its initial value. On the other hand, the current increases on illumination in Mg-doped ScN, as commonly seen in many semiconductors (Figure 1c). This positive photocurrent persists for several hours to several days, depending on the Mg concentration. Thus, NPC in degenerate ScN and PPC in Mg-doped ScN can be used as inhibitory and excitatory actions of a synapse, respectively, with the persistence in photoconductivity equated to the synaptic plasticity. Synaptic plasticity plays a vital role in creating memory. The higher the plasticity, the longer is the memory retention.

According to the Atkinson–Shiffrin model, memory development in the human brain has three main stages (as shown in Figure 1d).[46] First, the sensory organs sense the external stimuli and form sensory memory at the superficial layers of the brain. Paying attention to this input will transform it into STM lasting only for a few seconds to minutes. On rehearsal or revision, this data is stored as LTM that will be retained for several days, years, or a person's entire lifetime. This aspect of memory formation is successfully imitated in both the inhibitory and excitatory ScN-based artificial synapses. The effect of rehearsal is achieved by increasing the strength of the optical pulses by increasing their number, power, duration, and frequency. The STM, LTM, and transition from STM-to-LTM are executed in inhibitory (Figures 1e–h) and excitatory (Figures 1i–l) synapses with optical pulses. When the strength of the stimuli is low, the persistence in NPC and PPC is short (a few seconds), implying STM. With an increase in the stimuli strength in the form of more pulses, higher intensity, larger exposure time, and higher frequency, the persistence of photocurrent in both inhibitory and excitatory synapse increases that can be equated to their LTM. A clear transition from the STM-to-LTM is observed on all occasions, equivalent to rehearsing the information to remember it for an extended period.

Along with memory, learning is also an essential function of the brain and is the foundation for building brain-like computers. The change in conductivity due to the optical pulses is considered learning of the device, and restoration to the initial level is considered forgetting. In both inhibitory and excitatory ScN synaptic devices, the number of pulses required to reach a certain conductivity threshold reduces in consecutive cycles. Also, the rate of decay reduces with the number of cycles. The behavior of these devices follows Ebbinghaus's learning and forgetting curve.[47] According to this model, first-time learning takes much effort, and the learned information is forgotten over a while. However, re-learning takes less effort, and the learnt information is remembered for a longer time. In **Figure 2**a, ScN inhibitory synapses

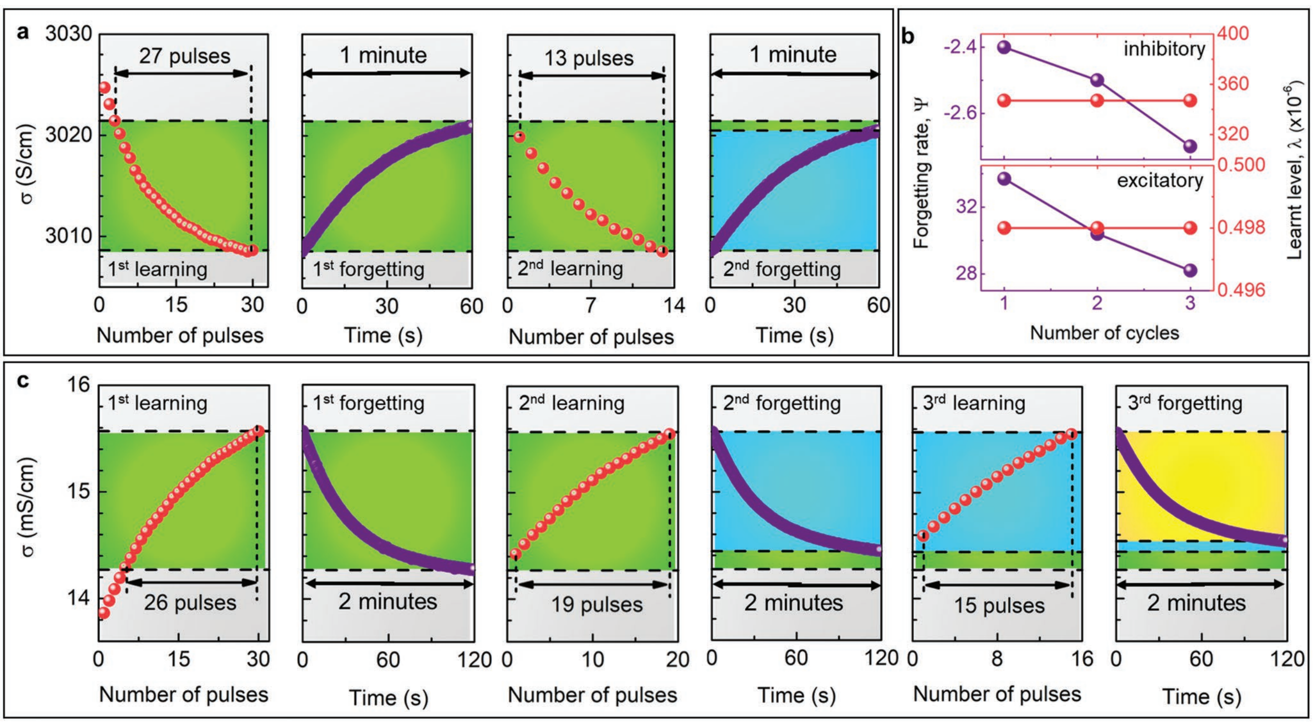

Figure 2. a) Learning and forgetting cycles in ScN inhibitory artificial synapse. b) Wickelgren's power law fitting clearly indicates the decrease in the forgetting rate with increase in number of learning cycles. c) Learning and forgetting cycles in Mg-doped ScN excitatory artificial synapse.

initially take 27 pulses for learning, and the learned information is forgotten in a minute. The second time learning requires only 13 pulses, and forgetting is slower than in the previous cycle. Similarly, in Mg-doped ScN excitatory synapses (Figure 2c), the number of pulses required in learning cycles reduces from 26 to 15 in three consecutive cycles, along with the decrease in the extent of forgetting. The learning–forgetting behavior in ScN can be better analyzed with Wickelgren's power law.[48] As per this law, the transient current (I) after the removal of stimuli (forgetting curves) can be fitted as a function of time (t) with the following equation:

$$I = \lambda(1+\beta t)^{-\psi} \tag{1}$$

where λ is the learned memory state, β is the scaling parameter, and ψ is the forgetting rate parameter. The λ and ψ obtained from the fitting of all forgetting curves are presented in Figure 2b. The forgetting rate parameter is negative because of the negative photoresponse of undoped ScN. From the same state of learnt memory, the forgetting rate parameter decreases with the increasing number of learning cycles in both excitatory and inhibitory artificial synapses. This clearly presents the learning ability of the ScN artificial optoelectronic synapses.

Post-synaptic current can be modulated as a function of the temporal pattern of the pre-synaptic signals in the brain. The frequency of the train of optical pulses arriving at the pre-synapse in the ScN synaptic devices alters the post-synaptic current, depending on the memory in the synapse stored due to preceding signals. In the train of optical pulses, the successive pulses can either increase (facilitate) or decrease (depress) the synaptic strength depending on the time interval between them. This well-known frequency dependence of PPF and PPD is exhibited by both inhibitory and excitatory ScN artificial synapses, as shown in **Figure 3**a,b, respectively. Here, on applying a set of 20 optical pulses at different frequencies switching between PPF and PPD is achieved. In the inhibitory synapse, PPF is achieved with optical pulses of 0.5 and 0.33 Hz, while PPD is achieved with 0.1, 0.2, and 0.05 Hz frequencies. Similarly, for excitatory synapse, optical stimuli at 0.5 and 0.2 Hz exhibit PPF, and optical stimuli at 0.05, 0.1, and 0.03 Hz exhibit PPD.

In addition, biological synapses also act as temporal filters for information processing based on stimulation frequency. Such a process is emulated in ScN artificial synaptic devices by measuring the post-synaptic current as a function of frequency of the optical stimuli. The frequency-dependent amplitude reduction (amplitude gain) of post-synaptic current in the inhibitory (excitatory) synapse is calculated as $|A_2/A_1| \times 100$. In ScN synapse, low-frequency signals are less inhibited, and hence their transmission to post-synaptic neurons is more probable (Figure 3c). In contrast, higher frequency signals have high amplitude gain in Mg-doped ScN and have higher transmittance probability (Figure 3d). Thus, ScN inhibitory synapse and Mg-doped ScN excitatory synapse act as low pass and high pass temporal filters, respectively.

While the above demonstrations consider stimulation of only pre-synapse, synaptic plasticity can also be varied by correlated stimulation of both pre- and post-synapses. The simple theory explaining this process in biological neurons is Hebb's postulate that states, "neurons that fire together wire together".[49] This concept can be emulated in ScN artificial synapses using two devices in series, one pre-synapse and the other post-synapse (**Figure 4**a). When the optical stimulus is incident on both the

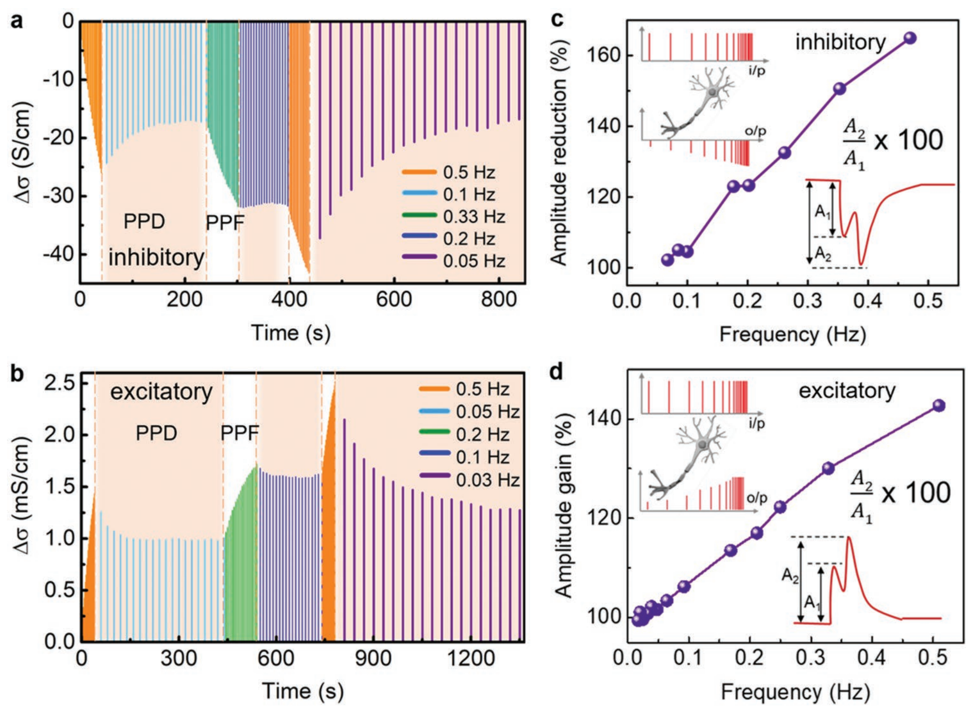

Figure 3. a,b) Frequency-dependent PPF and PPD in inhibitory ScN (a) and excitatory Mg-doped ScN (b) artificial synapse. PPF and PPD are marked in individual synapses with white and colored regions, respectively. c) The amplitude of current reduction increases at higher frequencies in inhibitory synapse functioning like a low pass filter. d) The gain amplitude increases at higher frequencies in the excitatory synapse, thus acting like a high pass filter.

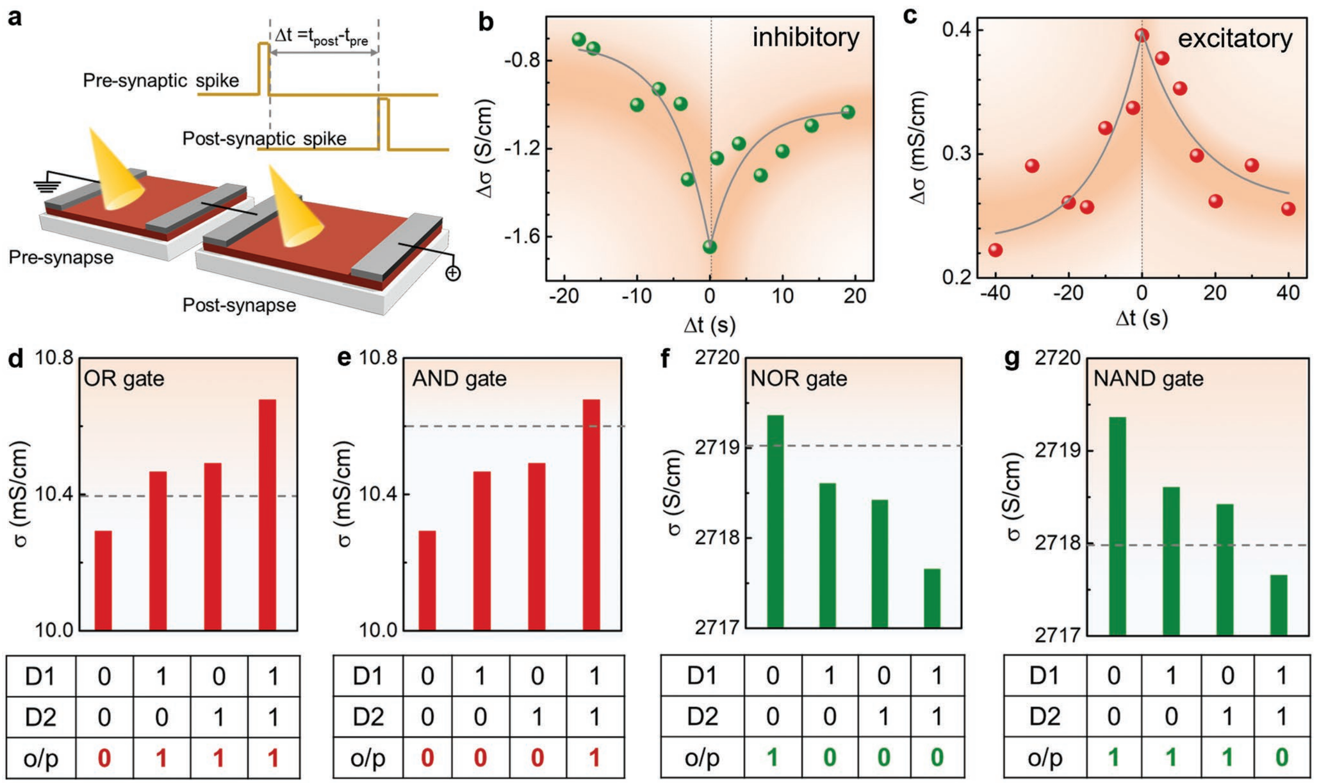

D1	0	1	0	1
D2	0	0	1	1
o/p	0	1	1	1

D1	0	1	0	1
D2	0	0	1	1
o/p	0	0	0	1

D1	0	1	0	1
D2	0	0	1	1
o/p	1	0	0	0

D1	0	1	0	1
D2	0	0	1	1
o/p	1	1	1	0

Figure 4. a) Schematic of measurements done with two devices connected in series. b,c) Symmetric STDP curve representing Hebbian learning in an inhibitory ScN synapse (b) and an excitatory Mg-doped ScN synapse (c). d) OR and e) AND logic operations demonstrated with two Mg-doped ScN devices in series. f) NOR and g) NAND logic operations demonstrated with two ScN devices in series.

synapses simultaneously ($\Delta t = 0$), the change in the net conductivity is maximum indicating a strong synaptic connection. As the time between the pre-synaptic and post-synaptic stimulus increases, the net change in synaptic conductivity reduces, as shown in Figure 4b,c. This symmetric curve representing the Hebbian law is one of the types of STDP, an essential phenomenon in determining the synaptic strength in biological neurons.

Further, information processing requires synapses to perform logic operations. The logic gates in the ScN artificial synapses are demonstrated with two devices connected in series (Figure 4a). If the optical pulse is incident on the device (D1 or D2), it is denoted as 1, else 0. The post-synaptic conductivity resulting from the optical stimuli is considered 1 if it is higher than a set threshold, else considered 0. The net conductivity is low when two Mg-doped ScN devices are connected in series without any input optical pulse. The optical stimuli on either or both the devices will increase the net conductivity due to their positive photoconducting nature. By setting a suitable threshold (as red dashed lines in Figures 4d,e), OR and AND gate operations are exhibited utilizing the excitatory synapses. Similarly, with inhibitory ScN synapses in series, NOR and NAND gate operations are demonstrated employing their negative photoconductivity (Figure 4f,g).

Since neuromorphic computers are required to exhibit high degrees of energy efficiency, measuring the energy consumption of the ScN artificial synapses is critical. The power density of the ScN excitatory and inhibitory synapses are calculated using the following equation:

$$\text{Power density}\left(\mathrm{W\,mm^{-2}}\right) = \frac{dW}{A} = V \times \frac{\Delta I}{A} \tag{2}$$

where W is the total power, A is the device area, V is the applied voltage across the electrodes (read voltage), and ΔI is the photocurrent. Calculations show that for a 1s optical stimuli, the power density of inhibitory synapse is 0.13 nW mm^{-2} at a read voltage of 20 mV, and that of the excitatory synapse is 0.65 nW mm^{-2} at 1 V read voltage. A relatively higher read voltage is used for excitatory synapse because of its higher resistivity. Though the previous works on optoelectronic synapses have reported the absolute energy consumption, their corresponding power density is found to be similar to the ScN synapses (more details in supporting information).

After demonstrating synaptic functionalities, we address the positive and negative photoconduction mechanisms in ScN that is vital for emulating excitatory and inhibitory synaptic activities. In Mg-doped ScN, the Fermi level is in the bandgap (**Figure** 5a). The positive photoconductivity results from the light-induced electron–hole pair generation and collection of the photogenerated carriers at the electrodes, similar to most conventional semiconductors' photoresponse. However, in pristine ScN, the Fermi level resides inside the conduction band by ≈100–250 meV due to the unintentional oxygen (n-type) incorporation (Figure 5b).[45] The photogenerated electrons are excited to the higher states in the conduction band (above E_F). The holes left behind in the valence band are captured by the trap states in the bandgap (V_N in ScN).[38] These captured holes act as charged

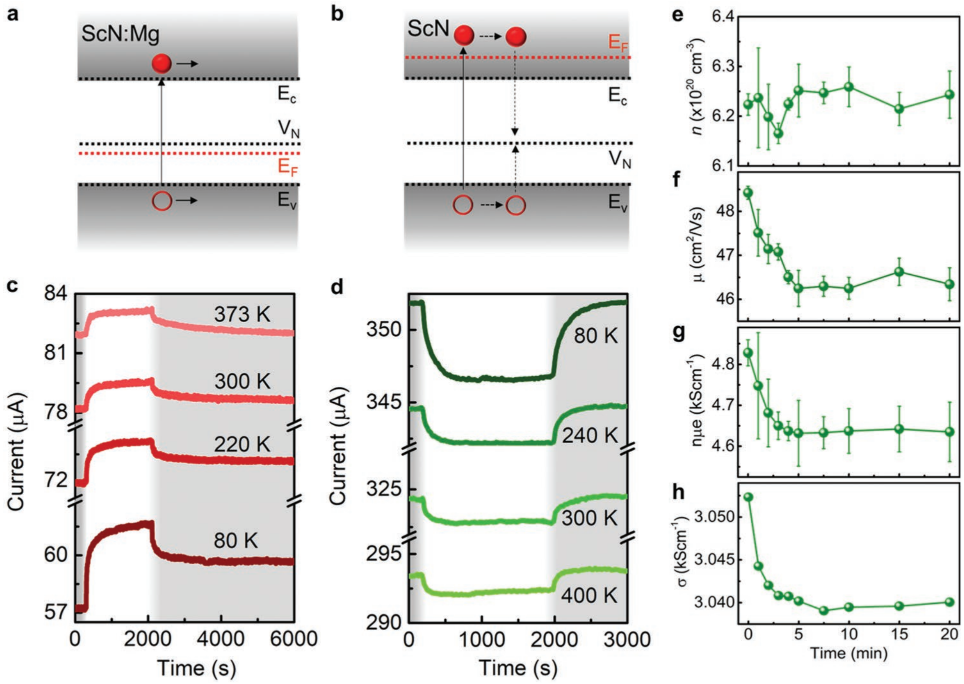

Figure 5. a) Band diagram of Mg-doped ScN where photogenerated carriers enhance the current in the device. b) Band diagram explaining the negative photoconductivity in pristine ScN where the photogenerated electrons are scattered by the charged scatterers formed at the sub-bandgap state (V_N). c,d) The nature of photoconductivity of pristine ScN (c) and Mg-doped ScN (d) measured at various temperatures reveals the robustness of this phenomenon. e) Carrier concentration and f) mobility of ScN measured with light being incident on the sample. The carrier concentration change is within the error bar while the mobility clearly decreases. g)The product $n\mu$ decreases, indicating a lowering of conductivity ($n\mu e$). h) The negative photoconductivity observed in pristine ScN matches well with (g) obtained from the photo-Hall effect.

scattering centers for photogenerated electrons, resulting in mobility reduction. Since the carrier concentration is already high, the net increase in the carrier density due to illumination is expected to be very small. This leads to a net decrease in conductivity ($ne\mu$) on illumination seen as negative photoconductivity. Photo-Hall measurement of the pristine ScN is performed to verify this mechanism. Results show that with light ON, the carrier concentration (n) (Figure 5e) remains almost unchanged, while the mobility (μ) (Figure 5f) decreases. The product of carrier concentration and mobility, defining the conductivity ($ne\mu$) (Figure 5g) follows the same trend as the photoconductivity (Figure 5h). It is important to note that the same model also successfully explained the negative photoconduction in degenerate InN.[50] Temperature-dependent photoresponse of pristine and Mg-doped ScN are measured in the 80–400 K temperature range (Figures 5c,d). The nature of photoresponse remains unaltered, while the magnitude of photoconductivity change increases at lower temperatures. A detailed analysis of the temperature-dependent growth and decay of photoconductivity is presented in the supporting information.

3. Conclusion

We present CMOS-compatible epitaxial group-III semiconducting ScN thin film optoelectronic synaptic devices that imitates the functionalities of biological synapses. Contrary to the previous demonstrations, both the inhibitory and excitatory synaptic functionalities are achieved in one host material, ScN, through carrier concentration control. STM, LTM, and transition from the STM-to-LTM are demonstrated as a function of the strength of the input optical pulse tuned by its duration, number, power, and frequency. Important synaptic activities like Ebbinghaus learning and forgetting cycles, frequency-dependent PPF, PPD, and temporal filtering of signals are also emulated. The Hebbian learning and logic gate operations are successfully achieved with two synaptic devices connected in a series configuration. Temperature-dependent photoresponse and photo-Hall measurements showed that the negative and positive photoresponse of degenerate ScN and Mg-(hole)-doped ScN depend strongly on the position of the Fermi level. Scattering of photogenerated carriers with charged defect centers are found to result in the negative photoconductivity in undoped degenerate ScN. This work paves the way for neuromorphic computer hardware development with a high-temperature stable epitaxial III-nitride semiconducting host material for practical device implementations.

4. Experimental Section

Single-crystalline scandium nitride thin films were deposited on 1 × 1 cm single-side polished MgO (001) substrates with reactive DC magnetron sputtering. The substrates were ultrasonicated in acetone and methanol before loading into the sputtering ultrahigh vacuum chamber with 1×10^{-9} Torr base pressure. An Ar:N_2 gas mixture with ratio of 9:2 was used, and the substrate temperature was maintained at 800 °C during all depositions. Sc target DC power was set to 100 W for pure ScN deposition, while it was varied in relation to Mg power during deposition of Mg-doped ScN to achieve different doping levels. The Mg-doped sample presented here was deposited at 125 W Sc and 6 W Mg power.

Indium wire (Alfa Aesar, 99.999% purity) was pressed onto the films to make Ohmic contacts. The current was measured using Kiethley 2450 with a read voltage of 0.02 and 1 V for ScN and ScN:Mg, respectively. The entire spectrum of the Newport Oriel Xe-arc lamp covering 250–2400 nm was incident on the sample without any filters or monochromator. The optical pulses were produced with manual shutter. All the photocurrent measurements were performed in vacuum environment at $\approx 5 \times 10^{-6}$ Torr. Janis cryostat was used for temperature-dependent photoconductivity measurement. Apart from intensity-dependent measurements, the photocurrent measurements were performed with 40 mW cm^{-2} optical intensity falling on the samples. Optical pulses of 1 s were used for all the measurements, except for pulse-duration-dependent measurement. The photo-Hall measurement was carried out with light from Xe-arc lamp shinning on the sample during the conventional Hall measurement.

Supporting Information

Supporting Information is available from the Wiley Online Library or from the author.

Acknowledgements

D.R. and B.S. acknowledge International Centre for Materials Science (ICMS) and Sheikh Saqr Laboratory (SSL) at JNCASR for support. B.S. acknowledges the Science and Engineering Research Board (SERB) of the Government of India, Start-Up Research Grant No. SRG/2019/000613 for financial support. D.R. thanks JNCASR for the fellowship. D.R. acknowledges SAMat research facilities. D.R. acknowledges Dr.Shashidhara Acharya and Krishna Chand Maurya for assistance in experimental work. A.I.K.P. and M.G. acknowledge the facilities of Sydney Microscopy and Microanalysis at The University of Sydney.

Conflict of Interest

The authors declare no conflict of interest.

Author Contributions

D.R. and B.S. conceived this project. D.R. deposited the thin films and performed materials characterization, device fabrication, and transport measurement experiments under the supervision of B.S.A. I.K.P. performed the TEM sample preparation. M.G. performed the TEM characterization. D.R. and B.S. analyzed the results. All authors discussed and contributed to the preparation of the manuscript.

Data Availability Statement

The data that support the findings of this study are available from the corresponding author upon reasonable request.

Keywords

artificial optoelectronic synapses, excitatory and inhibitory synapses, Hebbian learning, learning–forgetting, logic gates, long-term memory, potentiation–depression, scandium nitride, short-term

Received: August 25, 2022
Revised: November 7, 2022
Published online:

[1] D. V. Christensen, R. Dittmann, B. Linares-Barranco, A. Sebastian, M. L.e Gallo, A. Redaelli, S. Slesazeck, T. Mikolajick, S. Spiga, S. Menzel, I. Valov, G. Milano, C. Ricciardi, S.-J. Liang, F. Miao, M. Lanza, T. J. Quill, S. T. Keene, A. Salleo, J. Grollier, D. Marković, A. Mizrahi, P. Yao, J. J. Yang, G. Indiveri, J. P. Strachan, S. Datta, E. Vianello, A. Valentian, J. Feldmann, et al., *Neuromorph. Comput. Eng.* **2022**, *2*, 022501.
[2] K. Berggren, Q. Xia, K. K. Likharev, D. B. Strukov, H. Jiang, T. Mikolajick, D. Querlioz, M. Salinga, J. R. Erickson, S. Pi, F. Xiong, P. Lin, C. Li, Y. Chen, S. Xiong, B. D. Hoskins, M. W. Daniels, A. Madhavan, J. A. Liddle, J. J. McClelland, Y. Yang, J. Rupp, S. S. Nonnenmann, K.-T. Cheng, N. Gong, M. A. Lastras-Montaño, A. A. Talin, A. Salleo, B. J. Shastri, T. F. de Lima, et al., *Nanotechnology* **2021**, *32*, 012002.
[3] D. Graupe, *Principle of Artificial Neural Networks*, World Scientific, Singapore **2013**.
[4] D. A. Drachman, *Neurology* **2005**, *64*, 2004.
[5] J. von Neumann, *The Computer and the Brain*, Yale University Press, New Haven, CT, USA **1958**.
[6] R. Douglas, M. Mahowaldl, C. Mead, *Annu. Rev. Neurosci.* **1995**, *18*, 255.
[7] P. A. Merolla, J. V. Arthur, R. Alvarez-icaza, A. S. Cassidy, J. Sawada, F. Akopyan, B. L. Jackson, N. Imam, C. Guo, Y. Nakamura, B. Brezzo, I. Vo, S. K. Esser, R. Appuswamy, B. Taba, A. Amir, M. D. Flickner, W. P. Risk, R. Manohar, D. S. Modha, *Science.* **2014**, *345*, 668.
[8] Y. S. Yang, Y. Kim, in *2020 Int. SoC Design Conf. (ISOCC)*, IEEE, Piscataway, NJ, USA, **2020**, pp. 218–219.
[9] J. G. Cavazos, P. J. Phillips, C. D. Castillo, A. J. O'Toole, *IEEE Trans. Biom. Behav. Identity Sci.* **2021**, *3*, 101.
[10] C. D. Schuman, T. E. Potok, R. M. Patton, J. D. Birdwell, M. E. Dean, G. S. Rose, J. S. Plank, arXiv: 1705.06963v1, **2017**.
[11] D. B. Strukov, G. S. Snider, D. R. Stewart, R. S. Williams, *Nature* **2008**, *453*, 80.
[12] S. Deswal, A. Kumar, A. Kumar, *AIP Adv.* **2019**, *9*, 095022.
[13] S. Goswami, R. Pramanick, A. Patra, S. P. Rath, M. Foltin, A. Ariando, D. Thompson, T. Venkatesan, S. Goswami, R. S. Williams, *Nature* **2021**, *597*, 51.
[14] Z. Xiao, J. Huang, *Adv. Electron. Mater.* **2016**, *2*, 1600100.
[15] S. Seo, S.-H. Jo, S. Kim, J. Shim, S. Oh, J.-H. Kim, K. Heo, J.-W. Choi, C. Choi, S. Oh, D. Kuzum, H.-S. P. Wong, J.-H. Park, *Nat. Commun.* **2018**, *9*, 07572.
[16] W. Huh, D. Lee, C.-H. Lee, *Adv. Mater.* **2020**, *32*, 2002092.
[17] A. J. Arnold, A. Razavieh, J. R. Nasr, D. S. Schulman, C. M. Eichfeld, S. Das, *ACS Nano* **2017**, *11*, 3110.
[18] T. Ohno, T. Hasegawa, T. Tsuruoka, K. Terabe, J. K. Gimzewski, M. Aono, *Nat. Mater.* **2011**, *10*, 591.
[19] J. Li, C. Ge, J. Du, C. Wang, G. Yang, K. Jin, *Adv. Mater.* **2020**, *32*, 1905764.
[20] B. Bannur, G. U. Kulkarni, *Mater. Horiz.* **2020**, *7*, 2970.
[21] B. Gholipour, P. Bastock, C. Craig, K. Khan, D. Hewak, C. Soci, *Adv. Opt. Mater.* **2015**, *3*, 635.
[22] J. Feldmann, N. Youngblood, C. D. Wright, H. Bhaskaran, W. H. P. Pernice, *Nature* **2019**, *569*, 208.
[23] Y. Wang, L. Yin, W. Huang, Y. Li, S. Huang, Y. Zhu, D. Yang, X. Pi, *Adv. Intell. Syst.* **2021**, *3*, 2000099.
[24] S. E. Ng, J. Yang, R. A. John, N. Mathews, *Adv. Funct. Mater.* **2021**, *31*, 2100807.
[25] Y. Wang, Z. Lv, J. Chen, Z. Wang, Y. Zhou, L. Zhou, X. Chen, S.-T. Han, *Adv. Mater.* **2018**, *30*, 1802883.
[26] K. Pilarczyk, A. Podborska, M. Lis, M. Kawa, D. Migdal, K. Szaciłowski, *Adv. Electron. Mater.* **2016**, *2*, 1500471.
[27] J. Zhang, Y. Lu, S. Dai, R. Wang, D. Hao, S. Zhang, L. Xiong, J. Huang, *Research* **2021**, *2021*, 7131895.

[28] L. Yin, C. Han, Q. Zhang, Z. Ni, S. Zhao, K. Wang, D. Li, M. Xu, H. Wu, X. Pi, D. Yang, *Nano Energy* **2019**, *63*, 103859.
[29] J. Jiang, W. Hu, D. Xie, J. Yang, J. He, Y. Gao, Q. Wan, *Nanoscale* **2019**, *11*, 1360.
[30] S. Zhao, Z. Ni, H. Tan, Y. Wang, H. Jin, T. Nie, M. Xu, X. Pi, D. Yang, *Nano Energy* **2018**, *54*, 383.
[31] Y. Hou, X. Yu, Z. A. Syed, S. Shen, J. Bai, T. Wang, *Nanotechnology* **2016**, *27*, 455401.
[32] D. S. Tsai, W. C. Lien, D. H. Lien, K. M. Chen, M. L. Tsai, D. G. Senesky, Y. C. Yu, A. P. Pisano, J. H. He, *Sci. Rep.* **2013**, *3*, 2628.
[33] B. Biswas, B. Saha, *Phys. Rev. Mater.* **2019**, *3*, 020301.
[34] P. V. Burmistrova, J. Maassen, T. Favaloro, B. Saha, S. Salamat, Y. Rui Koh, M. S. Lundstrom, A. Shakouri, T. D. Sands, *J. Appl. Phys.* **2013**, *113*, 153704.
[35] M. J. Kappers, M. A. Moram, Y. Zhang, M. E. Vickers, Z. H. Barber, C. J. Humphreys, *Phys. B* **2007**, *401–402*, 296.
[36] M. Garbrecht, J. L. Schroeder, L. Hultman, J. Birch, B. Saha, T. D. Sands, *J. Mater. Sci.* **2016**, *51*, 8250.
[37] H. A. Al-Brithen, A. R. Smith, D. Gall, *Phys. Rev. B* **2004**, *70*, 045303.
[38] M. S. Haseman, B. A. Noesges, S. Shields, J. S. Cetnar, A. N. Reed, H. A. Al-Atabi, J. H. Edgar, L. J. Brillson, *APL Mater.* **2020**, *8*, 081103.
[39] D. Rao, B. Biswas, S. Acharya, V. Bhatia, A. I. K. Pillai, M. Garbrecht, B. Saha, *Appl. Phys. Lett.* **2020**, *117*, 212101.
[40] J. More-Chevalier, S. Cichoň, L. Horák, J. Bulíř, P. Hubík, Z. Gedeonová, L. Fekete, M. Poupon, J. Lančok, *Appl. Surf. Sci.* **2020**, *515*, 145968.
[41] D. Rao, B. Biswas, E. Flores, A. Chatterjee, M. Garbrecht, Y. R. Koh, V. Bhatia, A. I. K. Pillai, P. E. Hopkins, M. Martin-Gonzalez, B. Saha, *Appl. Phys. Lett.* **2020**, *116*, 152103.
[42] T. Ohgaki, K. Watanabe, Y. Adachi, I. Sakaguchi, S. Hishita, N. Ohashi, H. Haneda, *J. Appl. Phys.* **2013**, *114*, 093704.
[43] J. Casamento, J. Wright, R. Chaudhuri, H. Xing, D. Jena, *Appl. Phys. Lett.* **2019**, *115*, 172101.
[44] K. C. Maurya, D. Rao, S. Acharya, P. Rao, A. I. K. Pillai, S. K. Selvaraja, M. Garbrecht, B. Saha, *Nano Lett.* **2022**, *22*, 5182.
[45] B. Saha, J. A. Perez-Taborda, J.-H. Bahk, Y. R. Koh, A. Shakouri, M. Martin-Gonzalez, T. D. Sands, *Phys. Rev. B* **2018**, *97*, 085301.
[46] R. C. Atkinson, R. M. Shiffrin, *Psychol. Learn. Motiv.* **1968**, *2*, 89.
[47] H. Ebbinghaus, *Memory: A Contribution to Experimental Psychology*, Dover Publications, Mineola, NY, USA **1987**.
[48] J. T. Wixted, S. K. Carpenter, *Psychol. Sci.* **2007**, *18*, 133.
[49] Y. Munakata, J. Pfaffly, *Dev. Sci.* **2004**, *7*, 141.
[50] P.-C. Wei, S. Chattopadhyay, M. D. Yang, S.-C. Tong, J.-L. Shen, C.-Y. Lu, H.-C. Shih, L.-C. Chen, K.-H. Chen, *Phys. Rev. B* **2010**, *81*, 045306.